The Astrophysical Journal, 711:744–756, 2010 March 10 doi:10.1088/0004-637X/711/2/744

LABORATORY STUDIES ON THE IRRADIATION OF SOLID ETHANE ANALOG ICES AND IMPLICATIONS TO TITAN'S CHEMISTRY

Y. S. Kim[1], C. J. Bennett[1], Li-Hsieh Chen[1], K. O'Brien[2], and R. I. Kaiser[1]
[1] Department of Chemistry, University of Hawaii at Manoa, Honolulu, HI 96822, USA
[2] Department of Physics and Astronomy, Northern Arizona University, Flagstaff, AZ 86011, USA
Received 2009 November 12; accepted 2010 January 19; published 2010 February 18

ABSTRACT

Pure ethane ices (C_2H_6) were irradiated at 10, 30, and 50 K under contamination-free, ultrahigh vacuum conditions with energetic electrons generated in the track of galactic cosmic-ray (GCR) particles to simulate the interaction of GCRs with ethane ices in the outer solar system. The chemical processing of the samples was monitored by a Fourier transform infrared spectrometer and a quadrupole mass spectrometer during the irradiation phase and subsequent warm-up phases on line and in situ in order to extract qualitative (products) and quantitative (rate constants and yields) information on the newly synthesized molecules. Six hydrocarbons, methane (CH_4), acetylene (C_2H_2), ethylene (C_2H_4), and the ethyl radical (C_2H_5), together with *n*-butane (C_4H_{10}) and butene (C_4H_8), were found to form at the radiation dose reaching 1.4 eV per molecule. The column densities of these species were quantified in the irradiated ices at each temperature, permitting us to elucidate the temperature and phase-dependent production rates of individual molecules. A kinetic reaction scheme was developed to fit column densities of those species produced during irradiation of amorphous/crystalline ethane held at 10, 30, or 50 K. In general, the yield of the newly formed molecules dropped consistently for all species as the temperature was raised from 10 K to 50 K. Second, the yield in the amorphous samples was found to be systematically higher than in the crystalline samples at constant temperature. A closer look at the branching ratios indicates that ethane decomposes predominantly to ethylene and molecular hydrogen, which may compete with the formation of *n*-butane inside the ethane matrix. Among the higher molecular products, *n*-butane dominates. Of particular relevance to the atmosphere of Saturn's moon Titan is the radiation-induced methane production from ethane—an alternative source of replenishing methane into the atmosphere. Finally, we discuss to what extent the *n*-butane could be the source of "higher organics" on Titan's surface thus resembling a crucial sink of condensed ethane molecules.

Key words: astrochemistry – comets: general – infrared: planetary systems – methods: laboratory – molecular processes – planets and satellites: individual (Titan)

Online-only material: color figures

1. INTRODUCTION

Saturn's satellite Titan has a thick atmosphere comprised predominantly of nitrogen (N_2, 98.4%) and methane (CH_4, 1.4%; Niemann et al. 2005). The atmosphere is optically dense in the visible range of the electromagnetic spectrum due to orange-colored organic haze layers settled mostly in the stratosphere (McKay et al. 2001). Ethane (C_2H_6) presents a minor, but chemically significant component of the stratosphere; this molecule is likely produced by direct, solar-driven photodissociation of methane, as well as by indirect acetylenic catalysis in the atmosphere (Liang et al. 2007; Vinatier et al. 2007; Wilson & Atreya 2009). Once formed, ethane is transported downward and is thought to condense near the northern tropopause as predicted by photochemical and general circulation models of Titan (Rannou et al. 2006; Yung et al. 1984). A recent Cassini image captured a long-lasting northern polar cloud evidently composed of ethane aerosol particles with sizes of 1–3 μm (Griffith et al. 2006). Subsequently in the laboratory, the growth patterns of ethane aerosols were simulated (Bauerecker & Dartois 2009). These studies demonstrate that ethane condenses first in liquid phase onto buffer gases such as nitrogen (N_2). The nascent liquid droplets and aerosols then accelerate in growth to a few microns in diameter, in conjunction with morphological shifts toward the formation of crystalline solids. In the cold atmosphere of Titan, Hunten (2006) pointed out that ethane is likely sequestrated by organic hazes, seeding the cloud formation, sedimentation, and solid dropping onto Titan's ground. In fact, mass spectra taken at the Huygens landing site confirmed the ground-level ethane (Niemann et al. 2005). More recently, one interpretation of Cassini images suggested that ethane might exist in as liquid component of hydrocarbon-rich lake named Titan Ontario Lacus (Brown et al. 2008).

Besides the importance of ethane ices and aerosol particles, an understanding of the ethane chemistry is also relevant from the viewpoint of cometary chemistry. Here, ethane is considered as a valuable tracer of cometary ices tracking back to dense interstellar clouds in origin (Mumma et al. 1996). Since the first ground-based detection in comet C/1996 B2 Hyakutake (Mumma et al. 1996), ethane has been one of the most favorable targets after water (H_2O) for successive comet encounters (Russo et al. 2006). Multiple water-rich comets from the Oort Cloud such as C/2006 P1, 153P/Ikeya–Zhang, C/2001 A2, and C/1996 B2 are proven to contain high ethane abundances relative to methane, indicative of a common source of ethane production dating back to interstellar ices (Russo et al. 2001, 2009). Accordingly, Mumma et al. (1996) advocated the radiation processing of methane-rich ices on grain surfaces, coinciding the common production of ethane in several laboratory simulations by irradiating either pure methane ices (Bennett et al. 2006; Kaiser & Roessler 1998; Gerakines et al. 1996) or the mixtures in water (Moore & Hudson 1998). Finally, it should be noted that ethane plays an important role in the chemical processing of outer solar system bodies. For

instance, ethane can condense out from the tenuous atmospheres of Pluto and trans-Neptunian objects onto their surfaces (Bohn et al. 1994; Brown et al. 1997). Ethane abundances in nitrogen-dominant ices of Pluto remain at trace levels, while grains of solid ethane were recently discovered in a methane-dominant Kuiper Belt object 2005 FY9 (Sasaki et al. 2005; Brown et al. 2007). This underlines the necessity to understand the formation of ethane in our solar system.

To our best knowledge, only very few laboratory experiments have been conducted that investigate the interaction of ionizing radiation with pure ethane ices. UV photolysis of solid ethane at 77 K in the 1960s provided insights into potential decomposition pathways. Here, the photochemistry of solid ethane was driven by xenon (8.4 eV) and krypton (10.0 eV) resonance lines, reportedly yielding ethylene (C_2H_4), acetylene (C_2H_2), methane (CH_4), as well as heavier hydrocarbons such as *n*-butane (C_4H_{10}) and butene (C_4H_8) (Jackson et al. 1966; Scheer et al. 1962). However, the elective data analyses were based on non-spectroscopic methods including off-line and ex situ mass spectrometry and gas chromatograph; this could have altered the product spectrum significantly. Concerning high energy ion radiation, Strazzulla et al. (2002) prepared 180 nm-thick ethane ices at 12 K in a vacuum chamber with the base pressure ranging 10^{-7} torr. The amorphous ices were then irradiated with 30 keV He^+ at doses up to about 26 eV molecule^{-1}. The radiation-induced processes were monitored in situ by mid-infrared spectroscopy. The researchers were able to quantify the destruction rate of ethane and the formation rate of newly formed species such as ethylene, acetylene, and methane. No other products were mentioned, and mechanistical details on the formation of the new molecules remained elusive. Furthermore, ethane ices were bombarded with 15 keV N^+ ions; here, the researchers identified absorption bands attributable to C≡N-bearing species like hydrogen cyanide (HCN) and mono nitriles (Strazzulla et al. 2002). More recently, Compagnini et al. (2009) were particularly interested in the radiation-induced formation of polyynes. Using Raman spectroscopy, the researchers bombarded 2 μm thick ethane ices with 200 keV H^+ beams at the fluence reaching 5×10^{14} ions cm^{-2}, whereby they identified ethylene and acetylene. Another report concerning the laboratory radiation on solid ethane (C_2H_6) came into publication (Hudson et al. 2009). This group measured infrared band strengths of ethane absorption features in different phases prior to irradiation. Only amorphous ethane ices were reportedly irradiated with a beam of 0.8 MeV protons from a Van de Graaff accelerator. The radiation products were identified semi-quantitatively ranging from methane, acetylene, ethylene, *n*-butane to C_3H_x species ($x = 4$, 6, and 8).

However, these previous studies demonstrated that a systematic understanding of the radiation-induced processing of ethane ices is far from being complete. Here, we present a detailed experimental study on the processing of *amorphous* and *crystalline* ethane ices by energetic electrons over a broad temperature range from 10 to 50 K under oil-free ultrahigh vacuum conditions utilizing energetic electrons as a radiation source. Recall that energetic electrons are generated in the track of galactic cosmic-ray (GCR) particles (Bennett et al. 2005); they are further found in the magnetospheres of the giant planets (Cravens et al. 2005). Our goal is to elucidate not only the temperature and phase-dependent production rates of newly formed molecules, but also to untangle the underlying reaction mechanisms. Finally, we transfer our findings from the laboratory to the solar system and relate the irradiation time in the simulation experiments to the simulated radiation exposure of ethane in the particular example of Saturn's moon Titan.

2. EXPERIMENTAL DETAILS

The experiments were conducted in an ultrahigh vacuum chamber with the base pressure in the low 10^{-11} torr range (Bennett et al. 2004). Contamination-free vacuum conditions were rendered by a magnetically suspended turbo pump (1100 liters s^{-1}) backed by an oil-free scroll pump. A differentially pumped rotary platform, which holds a highly polished silver mirror as a substrate for the ice condensation, is positioned at the center of the chamber. Interfaced with the platform are a two-stage closed-cycle helium refrigerator and a feedthrough for a programmable temperature controller. The temperature of the silver crystal can be regulated with a precision of ±0.3 K between 10 K and 330 K. The ethane (C_2H_6) ices were prepared by depositing ethane (99.999%; Gaspro) through a glass capillary array positioned 5 mm in front of the silver substrate at 10 K. The deposition typically lasts 3 minutes at the ethane pressures of 1.5×10^{-8} torr. After the deposition, the infrared spectra of the solid samples were recorded in absorption—reflection–absorption (reflection angle $\alpha = 75^\circ$) either from 6000–400 cm^{-1} and 10,000–2000 cm^{-1} with 4 and 2 cm^{-1} resolution (Nicolet 6700 FTIR). The gas phase was monitored by a quadrupole mass spectrometer (Balzer QMG 420) operating in a residual gas analyzer mode with an electron impact ionization energy of 100 eV and a mass range of up to 200 amu.

Figure 1 depicts a mid-infrared spectrum of the ethane ices as deposited at 10 K. The vibrational assignments are compared with literature values in Table 1 (Comeford & Gould 1960; Hepp & Herman 1999). Our experimental conditions lead to the preparation of amorphous ethane at 10 K; this is evident from the lacking fine structures of the ν_6, ν_{11}, and ν_{12} bands in the range of 1600–700 cm^{-1}; in particular, the fine structures of the CH_3 deformation modes are missing (Tejada & Eggers 1976; Wisnosky et al. 1983a). Our amorphous spectra are also comparable to those recorded in liquid ethane droplets and aerosols leading to the formation of ethane clouds in Titan's atmosphere (Bauerecker & Dartois 2009; Curtis et al. 2008; Griffith et al. 2006; Sigurbjörnsson & Signorell 2008). The column density (molecules cm^{-2}) of ethane was estimated utilizing an integrated absorption coefficient of 1.9×10^{-18} cm molecule^{-1} for the ν_{12} at 820 cm^{-1} (Bennett et al. 2006). This leads to a column density of $(1.3 \pm 0.1) \times 10^{17}$ molecules cm^{-2}, translating into the ice thickness of 92 ± 5 nm after taking into account the reported density of solid ethane of 0.701 g cm^{-3} (Donnay & Ondik 1972). Furthermore, the phase transition of solid ethane was closely monitored by annealing the amorphous ices. Figure 2 depicts the spectral range of 1600–700 cm^{-1} that highlights the phase transition of amorphous ethane at 28 ± 1 K upon the gradient-heating to 30 K. During the period, the fine crystalline structures developed and became invariant to further temperature changes. Similarly, Wisnosky et al. (1983b) prepared a disordered solid ethane below 25 K that undergoes a phase transition at about 35 K to the crystalline II form upon heating. Note that amorphous ethane in our studies experiences the phase transition about 7 K below the reported temperature by Wisnosky et al. (1983b), likely attributable to our experiment performed at clean, ultrahigh vacuum conditions. As demonstrated previously in our group for the phase transitions in ammonia (NH_3), ultraclean conditions were imperative to extract accurate temperatures of phase transitions and of the

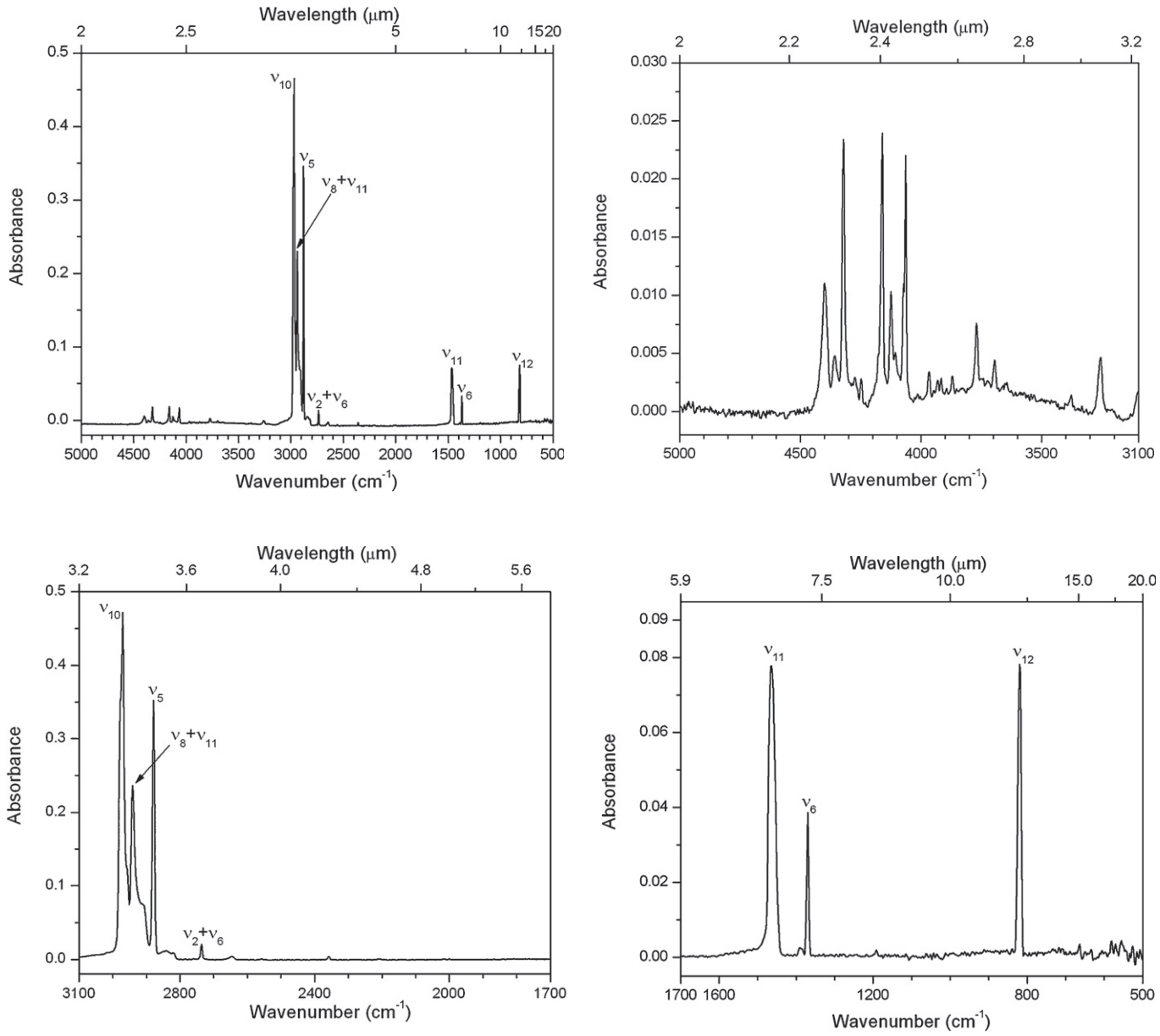

Figure 1. Mid-infrared spectrum of amorphous ethane ices (C_2H_6) recorded at 10 K. The assignments are compiled in Table 1.

crystallization (Zheng & Kaiser 2007). In our studies, we prepared a series of crystalline II ethane ices by means of depositing amorphous ethane at 10 K and subsequent annealing up to 50 K. A successive cooling from 50 K allowed preparing a crystalline II ethane held at 10 K.

The ethane ices were irradiated isothermally for 60 minutes with 5 keV electrons at a nominal beam current of 0 (blank), 20, or 100 nA. Multiple targets were selected to allow a systematic variation of the temperature and phase: amorphous ices at 10 K and crystalline ices at 10, 30, and 50 K. The electron beams were generated with an electron gun (Specs EQ 22–35) and scanned over the target area of 3.2 ± 0.3 cm^{-2}. Note that actual extraction efficiency of the electron gun is stated to be 78.8%, thus correcting the fluence down to 5.5×10^{14} electrons cm^{-2} hitting the target at a nominal current of 100 nA over 60 minutes. The electron trajectories and energy loss in ethane ices were then simulated using the CASINO code (Drouin et al. 2001). These calculations yield an averaged transmitted energy of the electrons at about 4.67 keV; this indicates that 330 eV per impinging electron has been transferred to the ices. This value corresponds to an average linear energy transfer (LET) of 3.6 ± 0.2 keV μm^{-1}, which is similar to the one of 3.2 ± 0.1 keV μm^{-1} obtained for 5 keV electron-irradiated methane ices studied earlier in our group (Bennett et al. 2006). Therefore, ethane ices receive an average dose of up to 1.4 ± 0.2 eV molecule^{-1} during the one hour exposure. After the irradiation is complete, the ices are kept isothermally for 60 minutes before being heated to 300 K with a gradient of 0.5 K min^{-1}. This allows the sublimed molecules to be detected by the quadrupole mass spectrometer.

3. RESULTS

3.1. Infrared Spectroscopy

First, we will investigate the radiation induced formation of new molecules in amorphous ethane ices at 10 K. Figure 3 displays the infrared spectra of amorphous ethane (C_2H_6) ices recorded at 10 K before and after the irradiation at 20 and

Table 1
Vibrational Assignments of Amorphous Ethane Ices (C_2H_6) at 10 K

Absorption (cm^{-1})	Literature Value[a] (cm^{-1})	Assignment[b]	Carrier
4399, 4321, 4162, 4125, 4073, 4064	...	...	Overtones/combinations
2972	2983	ν_{10}	CH_3 stretch
2941	2942	$\nu_8+\nu_{11}$	Combination
2879	2880	ν_5	CH_3 stretch
2736	2752	$\nu_2+\nu_6$	Combination
1464	1462	ν_{11}	CH_3 deform
1370	1369	ν_6	CH_3 deform
820	815	ν_{12}	CH_3 rock

Notes.
[a] Comeford & Gould 1960.
[b] Hepp & Herman 1999 with ν_7 in e_g symmetry.

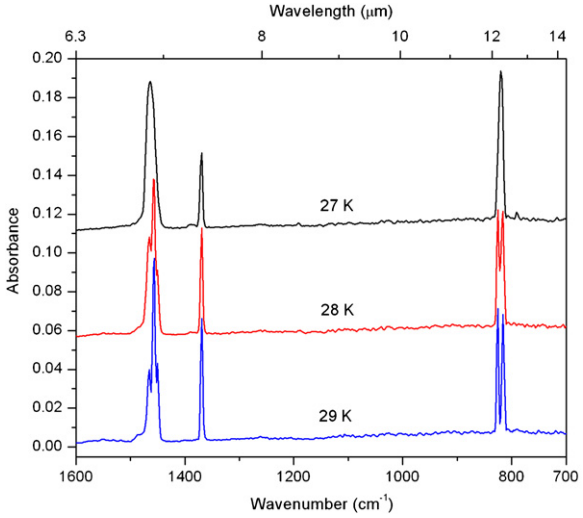

Figure 2. Temperature-dependent infrared spectra of solid ethane monitoring the transition of amorphous to crystalline II ethane at 28 ± 1 K.
(A color version of this figure is available in the online journal.)

100 nA. It is obvious that the radiation exposure leads to multiple new absorption features. A list of newly formed species is compiled along with the vibrational assignments in Table 2. Six hydrocarbons, methane (CH_4), acetylene (C_2H_2), ethylene (C_2H_4), and the ethyl radical (C_2H_5) together with *n*-butane (C_4H_{10}) and butene (C_4H_8), were identified; butene formation is greatly suppressed at 20 nA. In detail, methane fundamentals were monitored at 1300 (ν_4) and 3008 cm^{-1} (ν_3) (Moore & Hudson 2003; Gerakines et al. 2005). Absorptions of the ethyl radical arose at 532 cm^{-1} and 3108 cm^{-1}; these bands were assigned to the ν_9 and ν_{10} fundamentals, respectively. Both bands are indeed in good agreements with literature values (Bennett et al. 2006; Pacansky & Schrader 1983). The ethylene fundamental modes were detected at 949 (ν_7), 1434 (ν_{12}), and 3092 cm^{-1} (ν_9) in full accord with literature values (Bennett et al. 2006). Note that ν_7 of ethylene appeared quite blended with a group of absorptions near the 950 cm^{-1} region. The acetylene fundamentals were identified at about 740 (ν_5) and 3260 cm^{-1} (ν_3) in good agreement with Coustenis et al. (1999). An absorption at 734 cm^{-1} was assigned to the ν_{17} mode of *n*-butane in its *trans* form (C_{2h}); this corresponds to the carrier of CH_2 rocking vibrations in alkanes (Bohn et al. 1994). Three additional bands are identified for *n*-butane at 966 (ν_{35}), 2860, and 2957 cm^{-1} (ν_{12}, ν_{27}). A set of bands appearing only at 100 nA are assigned to butene (Barnes & Howells 1973; Comeford & Gould 1960). Upon heating, the ethane matrix sublimed in the range of 60–70 K, together with the volatile products methane, acetylene, and ethylene. However, heavier products, *n*-butane and butene, still remained on the substrate until 90 K. Figure 4 displays the infrared spectrum of the ices processed at 10 K and warmed up to 92 K. The major absorption features are attributable to *n*-butane in its *trans* form (Table 3). The absorption features of the carbon–hydrogen CH stretches are clearly seen in the region of 2900 cm^{-1}, as are those of group deformations at 1400, 950, and 730 cm^{-1} (Bohn et al. 1994). A set of asterisks are denoted for the contribution of butene (Gallinella & Cadioli 1997). We would like to stress that neither the methyl (CH_3) radical nor propane (C_3H_8), nor propylene (C_3H_6) was detected in any of our ethane experiments. Note that methyl radical and propane were monitored at 608 cm^{-1} (Bennett et al. 2006) and 750 cm^{-1} (Gerakines et al. 1996; Moore & Hudson 2003), respectively, in case of irradiated methane ices.

Hereafter, we would like to shift our attention to crystalline II ethane processed by the radiation exposure at 10, 30, and 50 K. Column densities of the new products are derived and compiled with reference to those recorded in the amorphous ices at 10 K (Table 4). Given the equivalent electron exposure, the crystalline ices held at different temperatures are less processed than the amorphous samples held at 10 K. The column densities of the newly formed molecules were systematically lower in the crystalline ices compared with the amorphous ices at the same temperature of 10 K. By quantitatively comparing the sum of product column densities derived, crystalline ethane is only 89% ± 5% as processed as the amorphous samples at 10 K. Second, we investigated how the production rates of the newly formed molecules in crystalline ethane ices depend on the target temperature. Here, lowering the substrate temperatures translates into the higher production yield. For instance, the methane production increases from (1.1 ± 0.2) $\times 10^{15}$ at 50 K to (1.5 ± 0.2) $\times 10^{15}$ molecules cm^{-2} at 10 K. Other volatiles such as acetylene and ethylene also exhibit sensible dependence on the target temperature with the yields ranging over 25%–75% and 44%–96% of the respective reference values. A heavier product such as *n*-butane in turn reveals a pattern of enhancement. Also listed in Table 4 are the total ion counts of gaseous methane and *n*-butane released during the warm-up phase after irradiation. The ion counts, which are proportional to the gas density of the newly formed molecules, are also normalized to the amorphous 10 K, tracking closely the trends observed in the solid phase in the particular case of methane. Especially at 50 K, the derived column density of methane

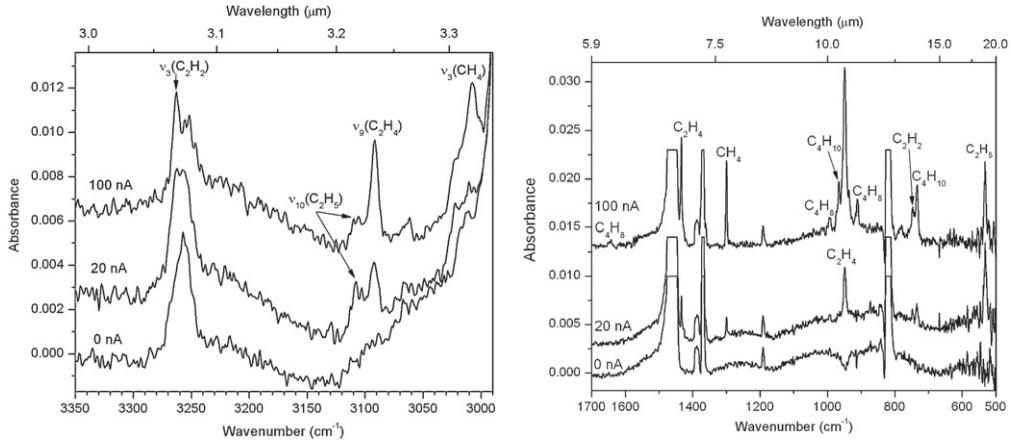

Figure 3. Infrared spectra of solid ethane at 10 K before (0 nA) and after irradiation (20, 100 nA). Ethane bands have been truncated to fit in the spectra. The assignments of the new species are compiled in Table 2.

Table 2
Infrared Absorption Features of the Newly Formed Species in Irradiated Ethane Ices

Absorption (cm^{-1})	Literature Value (cm^{-1})	Ref.	Assignment Species	Carrier
After 60 minutes irradiation (20, 100[a] nA) on amorphous C_2H_6 ice at 10 K				
532	534 / 540	1/ 2	C_2H_5	ν_9 (CH_2 out of plane)
734	731	3	C_4H_{10}	ν_{17} (CH_2 rock)
746 / 743[a]	769, 761, 746	4	C_2H_2	ν_5 (CCH bend)
911[a]	910	3	C_4H_8	(= CH_2 wag)
949	951	1	C_2H_4	ν_7 (CH_2 wag)
966[a]	964	3	C_4H_{10}	ν_{35} (CH_3 rock)
993[a]	993	3	C_4H_8	(HC = CH wag)
1300	1298	5	CH_4	ν_4 (deform)
1434	1435	1	C_2H_4	ν_{12} (CH_2 scissor)
1643[a]	1645	3	C_4H_8	(C = C stretch)
2860	...	...	C_4H_{10}	(CH_2 stretch)
2957	2968	3	C_4H_{10}	ν_{12}, ν_{27} (CH_3 str.)
3008[a]	3011	5	CH_4	ν_3 (stretch)
3092	3095	1	C_2H_4	ν_9 (CH_2 asym str.)
3108	3112	2	C_2H_5	ν_{10} (CH_2 asym str.)
3263	3267	1	C_2H_2	ν_3 (CH stretch)

Note.
[a]Additional features only at 100 nA current.
References. (1) Bennett et al. 2006; (2) Pacansky & Schrader 1983; (3) Comeford & Gould 1960; (4) Coustenis et al. 1999; (5) Moore & Hudson 2003.

reaches 73% of the solid phase, while the integrated ion counts 75% in gas phase after normalization. This observation itself demonstrates the adequacy of our dual detection scheme in quantifying volatile products using a Fourier transform infrared spectrometer (FTIR) and a quadrupole mass spectrometer. The last feature depicted in Figure 5 addresses the amorphization of crystalline ices that occurs during radiation exposure of crystalline ethane ices, reverse to the thermal process depicted in Figure 2. The identical spectral range of 1600–700 cm^{-1} now evidently monitors the shift on the crystalline features during the radiation exposure at 30 K. Note that the amorphization can also be monitored in the spectral regions of 4500–4000 and 3000–2800 cm^{-1}. In a qualitative sense, ethane absorptions at 2941 (ν_8+ ν_{11}) and at 2879 cm^{-1} (ν_5) appear least blended with amorphous features throughout the course of irradiation.

3.2. Mass Spectrometry

It is of interest to correlate the infrared observation with a mass spectroscopic analysis of the gas phase. Figure 6 displays ion count profiles of methane (CH_4), ethane (C_2H_6), and *n*-butane (C_4H_{10}) released during the warm-up phase after 0 nA and 100 nA irradiation of amorphous ethane at 10 K. It is important to stress that none of the newly formed species was detected in the residual gas analyzer during the actual irradiation phase, but only in the sublimation phases of the irradiated ices. The signal of $m/z = 30$ ($C_2H_6^+$) developed in the range of 60–70 K, so did the ion counts at $m/z = 16$ (CH_4^+). Note that ethane itself contributes to $m/z = 16$ due to electron impact ionization as shown in panel (a). The blank contribution in the irradiated ices is then subtracted for quantifying the methane signal (Table 4). The butane molecules, monitored at $m/z = 58$ ($C_4H_{10}^+$), sublimed at temperatures higher than 90 K and peaked at about 100 K.

4. DISCUSSION

4.1. Reaction Scheme

Having assigned the carriers of the newly formed molecules (Tables 2 and 3) and quantified the column densities of the newly

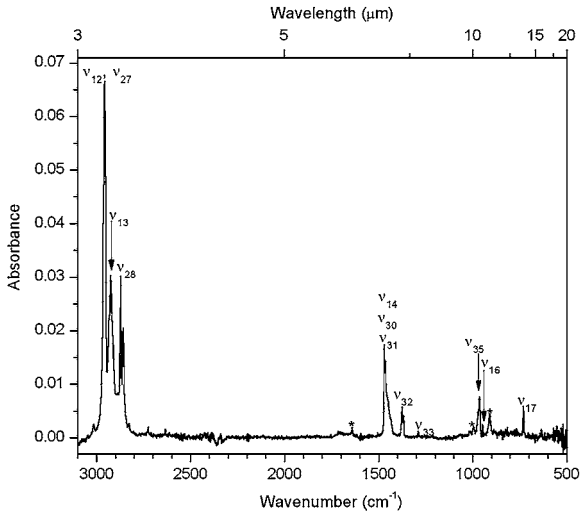

Figure 4. Infrared spectrum of the irradiated ethane ices warmed up to 92 K. The assignments of *n*-butane (C_4H_{10}) in *trans*-form are compiled in Table 3. A set of asterisks are marked for butene trace (C_4H_8).

Table 3
Vibrational Assignments of *n*-butane (C_4H_{10}) Recoded at 92 K During Warm-up Phase

Absorption (cm^{-1})	Literature Value[a] (cm^{-1})	Assignment[b]	Carrier
2958	2968	ν_{12}, ν_{27}	CH_3 asym stretch
2926	2930	ν_{13}	CH_2 asym stretch
2872	2870	ν_{28}	CH_3 sym stretch
2859	...	...	CH_2 sym stretch
1458	1461	ν_{14}, ν_{30}, ν_{31}	CH_3/CH_2 bend
1374	1379	ν_{32}	CH_3 deform
1290	1290	ν_{33}	CH_2 wag
968	964	ν_{35}	CH_3 rock
948	948	ν_{16}	CH_3 rock
731	731	ν_{17}	CH_2 rock

Notes.
[a] Comeford & Gould 1960.
[b] *Trans*-isomer; see http://webbook.nist.gov/chemistry.

formed molecules after the irradiation at different temperatures (Table 4), we are attempting now to elucidate the underlying reaction mechanisms how these species are synthesized in the ethane ices. For this purpose, a kinetic reaction scheme was developed (Figure 7) to fit the column densities of species produced during the irradiation of the amorphous/crystalline ethane (C_2H_6) ices held at 10, 30, or 50 K (Figure 8). A system of 13 coupled differential equations was numerically solved for each system (Frenklach et al. 1992) resulting in four sets of 13 rate constants k_1 to k_{13} (Table 5). In the case of the amorphous system at 10 K, two separate kinetic fits were derived for the temporal profiles to test the sensitivity of the fitting procedure with and without butene (C_4H_8) present. Table 6 summarized the relevant energetics of each process in the proposed kinetic scheme.

As described in Section 2, the temporal development of ethane column densities was traced by fitting Gaussian to the signature absorption at 820 cm^{-1} (ν_{12}). The hour-long radiation exposure to 5 keV electrons at a beam current of 100 nA caused a decrease in the column density of amorphous ethane from $(1.3 \pm 0.1) \times 10^{17}$ down to $(1.1 \pm 0.1) \times 10^{17}$ molecules cm^{-2}, which is equivalent to a $\sim 20\%$ decay. Considering the fluence of 5.5×10^{14} electrons cm^{-2} hitting the target, each impinging electron destroys 44 ± 13 molecules in the case of the amorphous ethane at 10 K. Similar to a radioactive decay, the ethane profile can be fit via a first-order decay (R1) with $k_a = (4.0 \pm 0.3) \times 10^{-4}$ s^{-1} for amorphous ice, while those of crystalline ethane were fit with $k_a = 3.3 \times 10^{-4}$ s^{-1} at 10 K, 2.3×10^{-4} s^{-1} at 30 K, and 1.4×10^{-4} s^{-1} at 50 K. The trend of a decreased destruction rate with increased temperature matched the enhanced destruction rates found at lower temperatures (Table 4).

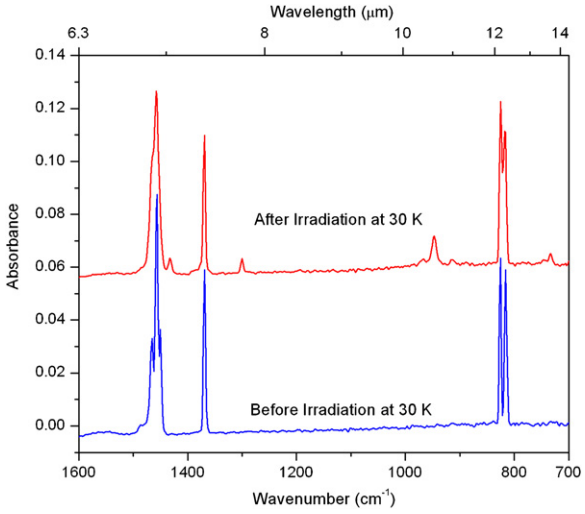

Figure 5. Infrared spectra monitoring amorphization of crystalline II ethane held at 30 K during radiation exposure, as reverse to the thermal process depicted in Figure 2.

(A color version of this figure is available in the online journal.)

$$[C_2H_6](t) = [C_2H_6](t = 0)e^{-k_a t} \quad (1)$$

Considering the unimolecular decomposition of the ethane reactant, five reactions (R2–R6) are considered to involve ethane during the radiolysis.

$$C_2H_6(X^1A_{1g}) \rightarrow C_2H_5(X^2A') + H(^2S_{1/2}) \quad (2)$$

$$C_2H_6(X^1A_{1g}) \rightarrow CH_4(X^1A_1) + CH_2(a^1A_1) \quad (3)$$

$$C_2H_6(X^1A_{1g}) \rightarrow C_2H_4(X^1A_g) + H_2\left(X^1\sum_g^+\right) \quad (4)$$

$$2\,C_2H_6(X^1A_{1g}) \rightarrow C_4H_{10}(X^1A_g) + H_2\left(X^1\sum_g^+\right) \quad (5)$$

$$H(^2S_{1/2}) + C_2H_6(X^1A_{1g}) \rightarrow C_2H_5(X^2A') + H_2\left(X^1\sum_g^+\right) \quad (6)$$

The ethyl radical (C_2H_5) is produced in reaction (R2) via an atomic hydrogen (H) loss channel via a simple bond rupture process, which Irle & Morokuma (2000) computed to be endoergic by 421 kJ mol^{-1} (4.36 eV); the energy for this endoergic process is supplied by the energy loss from the energetic electrons passing through the ethane ices with an average linear energy transfer (LET) of 3.6 ± 0.2 keV μm^{-1}. Note that the ethyl radical was monitored via its absorption at 3110 cm^{-1} (ν_{10}); the column densities reach a steady state after the initial rise, indicative of complex coupling with ethylene (C_2H_4) and *n*-butane (C_4H_{10}) formation (Figures 7 and 8). The rate constant, k_1, for the reaction (R2) is found to be 2.7×10^{-5} s^{-1} in the amorphous

Table 4
Temperature and Phase-dependent Production Yield in Irradiated Ethane Ices

Temperature, (K)	CH_4				C_2H_6	
	Solid Phase IR		Gas Phase QMS		Solid Phase IR	
	Column Density, (molecule cm^{-2})	Normalized, (%)	Ion Charge[a], (C)	Normalized, (%)	Column Density[b], (molecule cm^{-2})	
Amorphous 10	$(1.5 \pm 0.2) \times 10^{15}$	100	$(13.0 \pm 0.3) \times 10^{-10}$	100	$(1.3 \pm 0.1) \times 10^{17}$	...
Crystalline 10	$(1.5 \pm 0.2) \times 10^{15}$	100	$(12.1 \pm 0.3) \times 10^{-10}$	93	...	...
Crystalline 30	$(1.4 \pm 0.3) \times 10^{15}$	93	$(11.1 \pm 0.3) \times 10^{-10}$	85	...	...
Crystalline 50	$(1.1 \pm 0.2) \times 10^{15}$	73	$(9.7 \pm 0.3) \times 10^{-10}$	75	...	...
	C_2H_5		C_2H_4		C_2H_2	
Temperature, (K)	Column Density[c], (molecule cm^{-2})	Normalized, %	Column Density[d], (molecule cm^{-2})	Normalized, %	Column Density[e], (molecule cm^{-2})	Normalized, %
	Solid Phase IR					
Amorphous 10	$(1.5 \pm 0.5) \times 10^{15}$	100	$(10.6 \pm 1.9) \times 10^{15}$	100	$(0.4 \pm 0.2) \times 10^{15}$	100
Crystalline 10	$(1.3 \pm 0.6) \times 10^{15}$	87	$(10.2 \pm 1.4) \times 10^{15}$	96	$(0.3 \pm 0.1) \times 10^{15}$	75
Crystalline 30	$(0.7 \pm 0.1) \times 10^{15}$	47	$(8.5 \pm 0.7) \times 10^{15}$	80	$(0.2 \pm 0.0) \times 10^{15}$	50
Crystalline 50	...[f]	...	$(4.7 \pm 1.0) \times 10^{15}$	44	$(0.1 \pm 0.0) \times 10^{15}$	25
	C_4H_{10}				C_4H_8	
	Solid Phase IR		Gas Phase QMS		Solid Phase IR	
Temperature, (K)	Column Density[g], (molecule cm^{-2})	Normalized, %	Ion Charge[h], (C)	Normalized, %	Column Density[i], (molecule cm^{-2})	Normalized, %
Amorphous 10	$(9.9 \pm 1.4) \times 10^{15}$	100	$(5.8 \pm 0.0) \times 10^{-10}$	100	$(1.1 \pm 0.2) \times 10^{15}$	100
Crystalline 10	$(9.2 \pm 1.7) \times 10^{15}$	93	$(4.1 \pm 0.0) \times 10^{-10}$	71	...	...
Crystalline 30	$(7.6 \pm 1.4) \times 10^{15}$	77	$(3.5 \pm 0.0) \times 10^{-10}$	60	...	...
Crystalline 50	$(6.3 \pm 1.1) \times 10^{15}$	64	$(4.0 \pm 0.0) \times 10^{-10}$	69	...	...

Notes. 60 minutes irradiation of ethane (C_2H_6) ices with 5 keV, 100 nA. Crystalline ice values factored by 1.01–1.03.
[a] Ion currents of $m/z = 16$ integrated over scan time, less the contribution of blank ethane due to electron impact ionization.
[b] Initial column density before irradiation.
[c] Mean value derived from ν_9 and ν_{10} at about 530 and 3110 cm^{-1}, respectively, except at crystalline 30 K ν_{10} only.
[d] Mean value derived from ν_9 and ν_{12} at about 3090 and 1430 cm^{-1}, respectively.
[e] Mean value derived from ν_3 and ν_5 at about 3260 and 740 cm^{-1}, respectively.
[f] Upper limit of $(0.3 \pm 0.0) \times 10^{15}$ molecule cm^{-2} estimated.
[g] Main rotamer in *trans*-form only; mean value derived from ν_{17} and ν_{35} at about 730 and 960 cm^{-1}, respectively.
[h] Ion currents of $m/z = 58$ integrated over scan time.
[i] Mean value derived from C = C stretch and = CH_2 wag at about 1640 and 910 cm^{-1}, respectively.

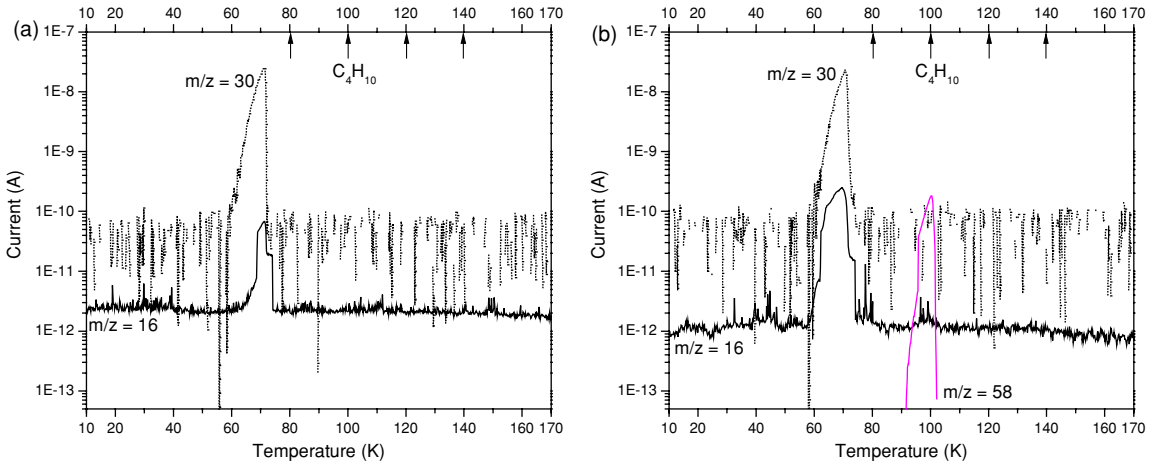

Figure 6. Ion-count profiles of methane (CH_4), ethane (C_2H_6), and butane (C_4H_{10}) released during warm-up phase after (a) 0 nA (b) 100 nA irradiation of amorphous ethane at 10 K.

(A color version of this figure is available in the online journal.)

ices at 10 K, while gradually decreasing in the crystalline ices at higher temperatures. The pattern of k_1 is also mirrored in final C_2H_5 column densities in Table 4. The production of methane (CH_4) in (R3) was also monitored in the gas phase photolysis of ethane (Okabe & McNesby 1961). Given the differences in the formation enthalpies of CH_4, CH_2 (a^1A_1) (Mebel et al. 1997), and C_2H_6, the reaction (R3) is found to be endoergic by 4.32 eV (Table 6); note that this process presents formally a barrier-less retro-insertion of singlet carbene, CH_2 (a^1A_1), into a carbon–hydrogen bond of methane. This process is similar to the retro-insertion of electronically excited oxygen atoms into a carbon–hydrogen bond of methane as observed in the unimolecular decomposition of the methanol molecule studied earlier in our group (Bennett et al. 2007); at 10 K, the latter process has a rate constant of about 6.2×10^{-6} s^{-1}, which is of the same magnitude as observed for the carbene plus methane channel in ethane. The temporal column densities of methane, monitored by the absorption at 1298 cm^{-1} (ν_4), develop linearly in the course of irradiation each experiment amplifying the interpretation of a unimolecular decomposition of ethane via first-order kinetics. The four set of rate constant, k_2, are found to be within $(2.5–3.9) \times 10^{-6}$ s^{-1}. A competing reaction (R4) presents formally a unimolecular decomposition of ethane via molecular hydrogen loss to form the ethylene molecule (C_2H_4). Two underlying pathways might compete in the formation of ethylene: a 1, 2 elimination of molecular hydrogen via a four-center mechanism or through an—unobserved and highly unstable—carbene intermediate, CH_3CH (a^1A_1), formed via a 1,1-molecular hydrogen loss following a three-center pathway. Irle & Morokuma (2000) stated that once the singlet CH_3CH (a^1A_1) is produced over the barrier, it rearranges immediately to ethylene (R4). Having identified three unimolecular decomposition pathways (R2–R4), we are comparing now their significance, i.e., the branching ratios. A closer look at the inherent rate constants for these processes suggests that reaction (R4) dominates: at all temperatures, ethane decomposes predominantly to ethylene and molecular hydrogen. According to Table 6, this is the energetically most favorable pathway requiring only 1.28 eV compared to 4.36 eV and 4.32 eV for reactions (R2) and (R3), respectively. At elevated temperatures, the formation of the ethyl radical plus atomic hydrogen (R2) presents the least important pathway, possibly because the effective formation of the ethyl radical is limited by the facile back-reaction of hydrogen atoms

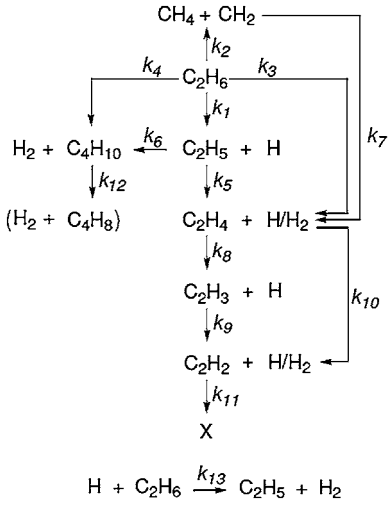

Figure 7. Reaction scheme used to fit temporal profiles of species produced during radiation exposure of amorphous/crystalline ethane ices.

in the matrix cage at higher temperatures which effectively recycles ethane.

We are turning now our attention to additional reaction pathways. An alternative route of the CH_3CH (a^1A_1) carbene inside the matrix is the reaction with a neighboring ethane molecule forming *n*-butane via the overall reaction (R5). The four sets of rate constants vary within $(0.2–1.3) \times 10^{-22}$ cm^2 $molecule^{-1}$ s^{-1}. Also, reaction (R6) is related to supra thermal (non-equilibrium) hydrogen atoms (Bennett et al. 2006). Due to a barrier to abstraction at 10 K, thermal hydrogen atoms cannot overcome this barrier. However, hydrogen atoms released in reaction (R2) can have an excess kinetic energy of up to a few eV (Bennett et al. 2006). This kinetic energy might be utilized to overcome the reaction barrier of (R6). Also, note that this channel seems energetically amenable considering that it is endoergic by only 6.3 kJ mol^{-1} (0.07 eV) after overcoming a barrier of 50.2 kJ mol^{-1} (0.52 eV; Kerkeni & Clary 2005). The rate constants of k_{13} are found to be $(0.6–1.5) \times 10^{-20}$ cm^2 $molecule^{-1}$ s^{-1}. Once produced in the reactions (R2) and (R6), the ethyl radical is subject to further radiolysis to yield ethylene (k_5), or alternatively to the self-dimerization to yield *n*-butane (k_6) with a neighboring

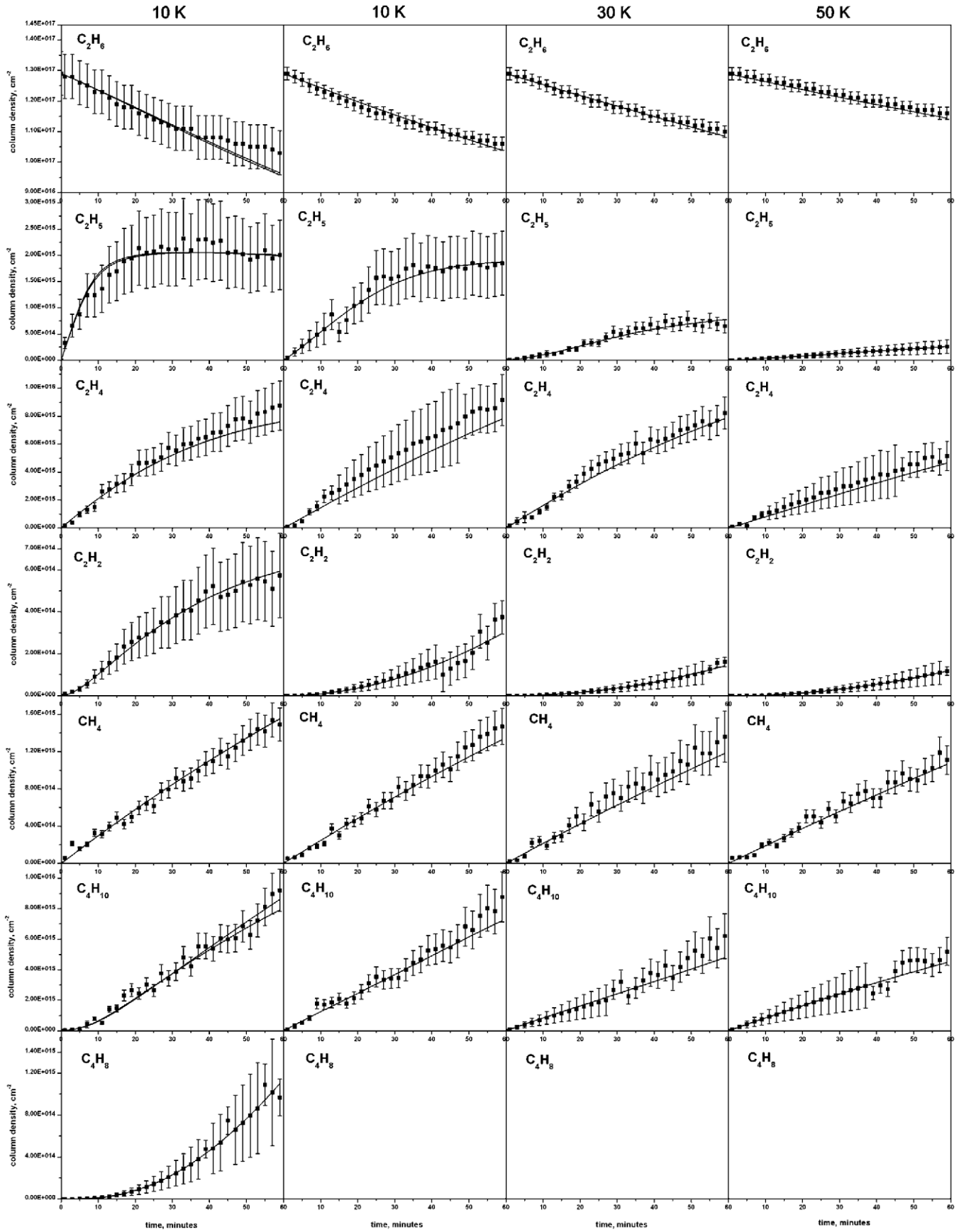

Figure 8. Fit of column densities of ethane (C_2H_6), ethyl radical (C_2H_5), ethylene (C_2H_4), acetylene (C_2H_2), methane (CH_4), and *n*-butane (C_4H_{10}). The two separate fits in the far left column are derived for the amorphous system at 10 K to test the sensitivity of the fitting procedure with and without butene (C_4H_8) present. The rest of the columns are for the crystalline system at 10, 30, and 50 K.

Table 5
Rate Constants Derived via Iterative Solution to the Reaction Scheme in Figure 7

Reaction	Rate Constant[a]			
	10 K Amorphous[b]	10 K Crystalline	30 K Crystalline	50 K Crystalline
$C_2H_6 \rightarrow C_2H_5 + H$	$k_1 = 2.7(2.7) \times 10^{-5}$	6.1×10^{-6}	8.7×10^{-7}	3.4×10^{-7}
$C_2H_6 \rightarrow CH_4 + CH_2$	$k_2 = 3.9(3.9) \times 10^{-6}$	3.2×10^{-6}	2.8×10^{-6}	2.5×10^{-6}
$C_2H_6 \rightarrow C_2H_4 + H_2$	$k_3 = 2.9(2.9) \times 10^{-5}$	1.8×10^{-5}	2.1×10^{-5}	1.0×10^{-5}
$2\,C_2H_6 \rightarrow C_4H_{10} + H_2$	$k_4 = 2.2(2.2) \times 10^{-23}$	1.3×10^{-22}	8.5×10^{-23}	8.6×10^{-23}
$C_2H_5 \rightarrow C_2H_4 + H$	$k_5 = 1.1(1.2) \times 10^{-7}$	7.8×10^{-8}	6.5×10^{-8}	7.7×10^{-8}
$2\,C_2H_5 \rightarrow C_4H_{10}$	$k_6 = 6.2(6.4) \times 10^{-19}$	1.7×10^{-19}	6.4×10^{-19}	4.6×10^{-20}
$2\,CH_2 \rightarrow C_2H_4$	$k_7 = 6.3(6.3) \times 10^{-18}$	1.6×10^{-17}	4.8×10^{-18}	8.4×10^{-18}
$C_2H_4 \rightarrow C_2H_3 + H$	$k_8 = 1.4(1.2) \times 10^{-7}$	2.7×10^{-8}	1.0×10^{-4}	5.4×10^{-8}
$C_2H_3 \rightarrow C_2H_2 + H$	$k_9 = 6.1(6.1) \times 10^{-8}$	8.4×10^{-7}	1.5×10^{-5}	2.2×10^{-7}
$C_2H_4 \rightarrow C_2H_2 + H_2$	$k_{10} = 2.9(2.9) \times 10^{-4}$	2.1×10^{-5}	7.6×10^{-6}	1.4×10^{-5}
$C_2H_2 \rightarrow X$	$k_{11} = 3.6(3.6) \times 10^{-3}$	3.5×10^{-11}	3.9×10^{-11}	3.9×10^{-11}
$C_4H_{10} \rightarrow (C_4H_8 + H_2)$	$k_{12} = 1.2 \times 10^{-6}/(8.5 \times 10^{-5})$	1.2×10^{-8}	2.3×10^{-8}	2.0×10^{-8}
$H + C_2H_6 \rightarrow C_2H_5 + H_2$	$k_{13} = 6.3(7.8) \times 10^{-21}$	6.1×10^{-21}	1.5×10^{-20}	1.4×10^{-20}

Notes.
[a] Units in s^{-1} (first order), except k_4, k_6, k_7, and k_{13} in cm^2 $molecule^{-1}$ s^{-1} (second order).
[b] Values in parenthesis derived with C_4H_8 column densities into account.

Table 6
Summary of Reaction Energetics Involved in this Study

Rate Constant	Reaction	$\Delta_R H$		ΔE_b		
		kJ mol^{-1}	eV	kJ mol^{-1}	eV	Ref.
k_1	$C_2H_6(X^1A_{1g}) \rightarrow C_2H_5(X^2A') + H(^2S_{1/2})$	421.0	4.36	...	...	1
k_2	$C_2H_6(X^1A_{1g}) \rightarrow CH_4(X^1A_1) + CH_2(a^1A_1)$	417.3	4.32	...	...	1, 2
k_3	$C_2H_6(X^1A_{1g})\,C_2H_4(X^1A_g) + H_2(X^1\sum_g^+)$	123.2	1.28	442.0	4.58	3
k_4	$2\,C_2H_6(X^1A_{1g}) \rightarrow C_4H_{10}(X^1A_g) + H_2(X1^1\sum_g^+)$	42.4	0.44	442.0	4.58	1, 3
k_5	$C_2H_5(X^2A') \rightarrow C_2H_4(X^1A_g) + H(^2S_{1/2})$	148.0	1.53	157.0	1.63	4
k_6	$2\,C_2H_5(X^2A') \rightarrow C_4H_{10}(X^1A_g)$	−363.6	−3.77	...	...	1
k_7	$2\,CH_2(a^1A_1) \rightarrow C_2H_4(X^1A_g)$	−763.8	−7.92	...	...	1, 2
k_8	$C_2H_4(X^1A_g) \rightarrow C_2H_3(X^2A') + H(^2S_{1/2})$	464.5	4.81	...	...	1
k_9	$C_2H_3(X^2A') \rightarrow C_2H_2(X^1\sum_g^+) + H(^2S_{1/2})$	147.0	1.52	163.0	1.69	4
k_{10}	$C_2H_4(X^1A_g) \rightarrow C_2H_2(X^1\sum_g^+) + H_2(X^1\sum_g^+)$	154.8	1.60	392.5	4.07	5
k_{11}	$C_2H_2(X^1\sum_g^+) \rightarrow X$	...	...	...	...	...
k_{12}	$C_4H_{10}\,(X^1A_g) \rightarrow (C_4H_8 + H_2(X^1\sum_g^+))$	125.0	1.30	439[a]	4.55[a]	1, 3
k_{13}	$H(^2S_{1/2}) + C_2H_6(X^1A_{1g}) \rightarrow C_2H_5(X^2A') + H_2(X^1\sum_g^+)$	6.3	0.07	50.2	0.52	6

Notes. The reaction enthalpy ($\Delta_R H$) given along with any additional barrier (ΔE_b).
[a] Estimated from H_2 elimination channel of propane (C_3H_8) in Irle & Morokuma (2000).
References. (1) see http://webbook.nist.gov/chemistry; (2) $\Delta_f H$ (CH_2, $^1A_1$) = 4.23 eV derived from Mebel et al. 1997; (3) Irle & Morokuma 2000; (4) Bennett et al. 2006; (5) Jensen et al. 1994; (6) Kerkeni & Clary 2005.

radical. Further, we had to include one channel accounting that methylene (CH_2), a co-product of reaction (R3), self-dimerizes (k_7) to form ethylene. Furthermore, ethylene (C_2H_4) can be radiolyzed stepwise (k_8 and k_9), or in a concerted way (k_{10}), to yield acetylene (C_2H_2) (Bennett et al. 2006; Jensen et al. 1994). The last reaction worthy of mentioning is the radiolysis-induced formation of heavier molecular compounds "X" from acetylene (C_2H_2), which Compagnini et al. (2009) referred to as the route of forming carbon nano wires.

4.2. Energetics

As compiled in Section 4.1, solid ethane (C_2H_6) can be radiolyzed via multiple reactions that permit us to extract the minimum energy required to destroy each ethane molecule. The reaction (R2) is an atomic hydrogen (H) loss channel and requires 4.36 eV; the reaction (R3) symbolizes a methane-forming channel needing 4.32 eV; the reaction (R5) proceeds via a molecular hydrogen (H_2) loss of ethane having the barrier of 4.58 eV (Table 6). With the focus on the amorphous system at 10 K, the hour-long exposure has destroyed ethane (C_2H_6) totaling $(24 \pm 7) \times 10^{15}$ molecules cm^{-2}. Given the fluence of 5.5×10^{14} electrons cm^{-2} hitting the target, each electron is found to destroy 44 ± 13 ethane molecules. Considering the energetics, these processes need 197 ± 58 eV to be transferred to the sample by each electron. Recall the CASINO code estimate that 330 eV will be transferred to the sample per electron. This implies that the contribution of ethane destruction accounts for 60% of the total transferred energy. Considering the overall production of molecules and the energetics (Table 7), we can sum up the total energy required to produce the newly formed molecules to be 248 ± 44 eV per electron being transferred to the matrix. This is equivalent to a fraction of 75% of the total transferred energy by each electron as computed via the CASINO code. The remaining energy is released to the phonons and vibrational modes of individual molecules.

Table 7
Summary of Temporal Changes in Column Density of the Observed Species at the End of Irradiation—10 K Amorphous Only

Species	Absorption (cm^{-1})	A[a] (cm molecule^{-1})	Column Density Changed ($\times 10^{15}$ molecules cm^{-2})	Molecules Produced per Electron[b]	Minimum Energy Required per Molecule (eV)	Total Energy Translated to Matrix per Electron (eV)	Carbon Atoms Produced ($\times 10^{15}$ cm^{-2})
C_2H_6	820	1.9×10^{-18}	-24 ± 7	-44 ± 13	4.52[c]	-197 ± 58	-48 ± 14
CH_4	1300	7.0×10^{-18}	1.5 ± 0.2	2.7 ± 0.4	4.32	11.8 ± 1.6	1.5 ± 0.2
C_2H_5	3110, 530	3.2×10^{-18}, 9.3×10^{-18}	1.5 ± 0.5[d]	2.7 ± 0.9	4.36	11.9 ± 4.0	3.0 ± 1.0
C_2H_4	3090, 1430	1.7×10^{-18}, 1.6×10^{-18}	10.6 ± 1.9[d]	19.3 ± 3.5	5.99	115.4 ± 20.7	21.2 ± 3.8
C_2H_2	3260, 740	1.3×10^{-17}, 3.0×10^{-17}	0.4 ± 0.2[d]	0.8 ± 0.3	10.06	7.9 ± 2.7	0.9 ± 0.3
C_4H_{10}	960, 730	1.8×10^{-18}, 8.8×10^{-19}	9.9 ± 1.4[d]	18.0 ± 2.6	4.58	82.4 ± 11.7	39.6 ± 5.6
C_4H_8	1640, 910	1.3×10^{-18}, 6.0×10^{-18}	1.1 ± 0.2[d]	2.0 ± 0.4	9.13	18.3 ± 3.3	4.4 ± 0.8
Total	...	...	25.0 ± 4.4	45.5 ± 7.9	...	247.7 ± 43.9	70.6 ± 11.7

Notes.
[a] A value(s) of C_2H_6 / C_2H_5 from Bennett et al. 2006, of CH_4 from Gerakines et al. 2005, of C_2H_4 / C_2H_2 / C_4H_{10} from Bohn et al. 1994, and of C_4H_8 from Gallinella & Cadioli 1997.
[b] Fluence of 5.5×10^{14} electrons cm^{-2} hitting the target over 60 minutes irradiation.
[c] Mean value of weighing CH_4, C_2H_5, and C_4H_{10} production into account.
[d] Mean value derived from two absorptions.

4.3. Carbon Budget

In Section 4.2, we discussed the energetics underlying the electron irradiation of amorphous ethane ices at 10 K. Briefly in this section, we would like to address the issue of the carbon budget related to the particular experiment. In the course of irradiation, ethane column densities decrease by $(24 \pm 7) \times 10^{15}$ molecules cm^{-2}, while the combined column densities of the products reaching $(25 \pm 4) \times 10^{15}$ molecules cm^{-2}; the contribution of *n*-butane (C_4H_{10}) and butene (C_4H_8) together equal about 11×10^{15} molecules cm^{-2}, or 44% of the combined (Table 7). As far as stoichiometry is concerned with the experiment, *n*-butane could be a likely source of overproduction, due to the fact that *n*-butane is produced from the dimerization of ethane, by the amount of 5.5×10^{15} molecules cm^{-2}, or 22×10^{15} carbons cm^{-2}. This first-order approximation holds well in that it accounts for the differences in the number of carbon atoms lost by ethane and gained by the sum of six products (Table 7). It is still worth recognizing some degrees of intrinsic errors associated with deriving the column density of each species—fitting Gaussian to an absorption band, the absorption coefficient of which is either an experimental gas phase or a theoretical value reported in the literatures. Within the scope of this paper, the carbon budget is deemed to be conserved by about 30% during of irradiation.

4.4. Comparison to Previous Experiments

We now would like to compare our results to those of previous irradiation experiments on pure solid ethane (C_2H_6). Currently, amorphous/crystalline II ethane ices are prepared under ultrahigh vacuum conditions and processed by 5 keV electrons at 10, 30, or 50 K. In 1960s, an undefined phase of solid ethane was prepared at 77 K and processed by vacuum ultraviolet photons (Jackson et al. 1966; Scheer et al. 1962). Although fractional conversions were reported, volatile products were assigned to match those from our experiments. In contrast, 30 keV He^+ irradiation by Strazzulla et al. (2002) allowed the destruction of amorphous ethane at 12 K over 70% at the radiation dose reaching 26 eV molecule^{-1}. The reported temporal profiles indicate that as radiation doses reach this level, methane (CH_4) may become a dominant product over ethylene (C_2H_4) or acetylene (C_2H_2), along with a polymer-like residue. However, other radiation products such as *n*-butane (C_4H_{10}) were not identified. Hudson et al. (2009) irradiated amorphous ethane at about 20 K with 0.8 MeV protons from a Van de Graaff accelerator. The radiation products were assigned similar to ours other than C_3H_x ($x = 4$, 6, and 8). The presence of C_3H_x was also suggested to result from butane decomposition; due to the low radiation doses in our experiments, this pathway was not observed. This group determined the radiation dose (22 eV molecule^{-1}) destroying 33% of their ethane molecules; this strongly contrasts our experiments conducted at average dose of only 1.4 eV molecule^{-1}.

5. ASTROPHYSICAL IMPLICATIONS

Recent spectroscopic images from the Cassini spacecraft have provided a topological view on ethane (C_2H_6) condensed in the lower atmosphere and the surface of Saturn's satellite Titan (Brown et al. 2008; Griffith et al. 2006; Lorenz et al. 2008). Ethane aerosol in sizes of 1–3 μm was reportedly an effective element of a massive cloud capping the northern hemisphere (Griffith et al. 2006). Brown et al. (2008) discovered a surface organic lake, Titan Ontario Lacus, where ethane is identified to be a liquid component. Higher molecular weight species were postulated, but could not be identified spectroscopically on Titan. Based on our experiments, these higher order products could likely be butane (C_4H_{10}) and/or butene (C_4H_8) formed via cosmic-ray processing of ethane. Dark dunes of "sand" are also thought to cover up to 20% of Titan's surface (Lorenz et al. 2008), where the sequestrated and radiolytically processed ethane could be the main ingredient (Hunten 2006). Mousis & Schmitt (2008) alternatively suggested that the surface ethane could have been sequestrated through pores of cryovolcanic lavas into the subsurface of Titan over periods of about 10^9 years. The resulting clathrate formation could influence the process of cryovolcanic activity leading to episodic methane

outgassing to the surface (Wilson & Atreya 2009). As yet, little information has surfaced on the radiation-induced processing of the condensed ethane at the altitudes. Galactic cosmic radiation has been suggested as a mechanism for creating the ionosphere of Titan, where the Sun's radiation is effectively absorbed by organic hazes in the stratosphere (Molina-Cuberos et al. 1999; Sagan & Thompson 1984; Whitten et al. 2007). This was evident during the Huygens probe descent to the Titan surface in 2005. A pair of ion-counters onboard indeed detected an ionized layer peaking at 65 km altitude (López-Moreno et al. 2008).

Below this altitude, a small flux of primary/secondary cosmic rays is expected to arrive at the surface (Wilson & Atreya 2009). By applying the validated O'Brien algorithm (Molina-Cuberos et al. 1999), the energy deposition on Titan's surface led by muon fluxes is about 4.6×10^7 eV cm^{-2} s^{-1} invariant to seasonal solar activities; the effects of muons and energetic electrons on ices are comparable (Molina-Cuberos et al. 1999). Considering our radiation source of energetic electrons, generated in the track of energetic GCR particles, each electron transfers 330 eV to the ethane ices. Considering the total flux of 5.5×10^{14} electrons cm^{-2} in our experiments, the ethane ices are exposed to 1.8×10^{17} eV cm^{-2} during the laboratory experiments. Therefore, our radiation exposure is equivalent to an actual exposure time of Titan's surface of about 125 years. At the corresponding radiation dose of 1.4 eV molecule^{-1}, solid ethane is radiolyzed to yield an array of products led by methane (CH_4), ethylene (C_2H_4), and *n*-butane (C_4H_{10}). Of particular relevance to the Titan atmosphere is the radiolysis-induced methane production—an alternative source of replenishing methane into Titan's atmosphere. Production rates of methane determined at 10, 30, and 50 K (Table 4) provide the basis for linear extrapolation toward the Titan surface temperature at 94 K (Figure 9). The resulting rate at 94 K is found to be $(7.2 \pm 2.3) \times 10^{14}$ molecules cm^{-2} equivalent to 0.6% of the initial ethane column density, $(1.3 \pm 0.1) \times 10^{17}$ molecules cm^{-2}. Should the equal amount of ethane be constrained on the Titan surface and bombarded by cosmic rays at the energy flux reaching 4.6×10^7 eV cm^{-2} s^{-1} instead, our laboratory data suggest the methane production rate to be 1.8×10^5 molecules cm^{-2} s^{-1} at 94 K, i.e., the production rate of methane at 4.9×10^{-21} kg cm^{-2} s^{-1}. Corresponding column density of *n*-butane product is about 4.4 times higher (Figure 9), i.e., 8.2×10^5 molecules cm^{-2} s^{-1}; this translates to the absolute rate of about 7.9×10^{-20} kg cm^{-2} s^{-1}. Therefore, over geological timescales, a significant fraction of ethane could be recycled into methane; further, ethane can be converted easily to a higher molecular weight product: *n*-butane. Further models of Titan will show if the replenishment of methane will be sufficient to account for the actual in situ observations. In addition, prospective models shall investigate if the production of *n*-butane can account for the "missing" global ethane lakes. Recall that previous models suggested that Titan's surface should be covered by ethane lakes about 1000 m deep (Lunine et al. 1983); this global coverage was clearly not observed by the Cassini–Huygens mission. Consequently, the conversion of ethane to solid *n*-butane might account for the failed observation of a global ethane ocean on Titan; *n*-butane, which is solid at Titan's surface temperature of 94 K, could also present a building block for the "organic" sand dunes as observed by Cassini (Radebaugh et al. 2008).

Finally, cometary volatiles of acetylene (C_2H_2), methane, and ethane are important tracers to constrain a comet formation mechanism (Russo et al. 2006). During a typical comet encounter, infrared emission lines of the volatiles are often surveyed using a high-resolution spectrometer, providing access to the production rates and relative abundances tracing possibly back to interstellar clouds in origin. The Oort Cloud comets are chemically processed by GCR radiation, many of which are often detected to reveal high ethane abundances relative to methane (Russo et al. 2001, 2009)—an indicator to common production mechanism such as the radiation processing of methane-rich ices on grain surfaces (Mumma et al. 1996). In the laboratory radiation of solid ethane, two volatiles of methane and acetylene are found to evolve via two separate pathways. *n*-butane (C_4H_{10}), a heavier volatile, is also notably produced in solid phase during irradiation. The subsequent warm-up allows monitoring the ion-count profile at $m/z = 58$ ($C_4H_{10}^+$) released to gas phase, the process perceivable when ethane-rich comets enter the inner solar system.

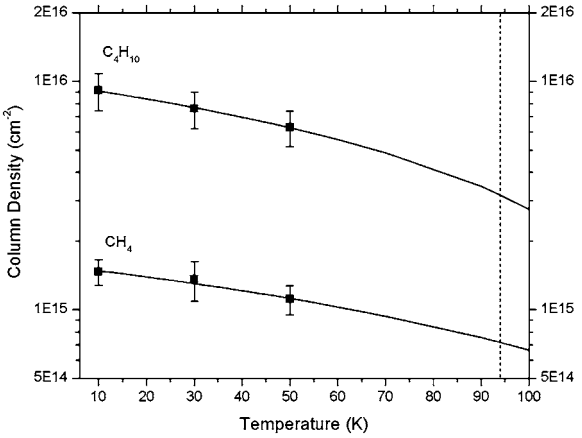

Figure 9. Production yield of methane (CH_4) and butane (C_4H_{10}) linearly extrapolated toward the Titan surface temperature (94 K) from the basis of those determined at lower temperatures (Table 4). The resulting yield of methane and butane at 94 K is found to be $(7.2 \pm 2.3) \times 10^{14}$ and $(3.2 \pm 1.9) \times 10^{15}$ molecules cm^{-2} within 1σ error level, respectively.

The experimental work was supported by the Chemistry Division of the US National Science Foundation within the framework of the Collaborative Research in Chemistry (CRC) Program (NSF-CRC CHE-0627854).

REFERENCES

Barnes, A. J., & Howells, J. D. R. 1973, J. Chem. Soc. Faraday Trans. II, 69, 532
Bauerecker, S., & Dartois, E. 2009, Icarus, 199, 564
Bennett, C. J., Chen, S.-H., Sun, B.-J., Chang, A. H. H., & Kaiser, R. I. 2007, ApJ, 660, 1588
Bennett, C., Jamieson, C., Mebel, A. M., & Kaiser, R. I. 2004, Phys. Chem. Chem. Phys., 6, 735
Bennett, C. J., Jamieson, C. S., Osamura, Y., & Kaiser, R. I. 2005, ApJ, 624, 1097
Bennett, C. J., Jamieson, C. S., Osamura, Y., & Kaiser, R. I. 2006, ApJ, 653, 792
Bohn, R. B., Sandford, S. A., Allamandola, L. J., & Cruikshank, D. P. 1994, Icarus, 111, 151
Brown, M. E., Barkume, K. M., Blake, G. A., Schaller, E. L., Rabinowitz, D. L., Roe, H. G., & Trujillo, C. A. 2007, AJ, 133, 284
Brown, R. H., Cruikshank, D. P., Pendleton, Y., & Veeder, G. J. 1997, Science, 276, 937
Brown, R. H., et al. 2008, Nature, 454, 607
Comeford, J. J., & Gould, J. H. 1960, J. Mol. Spectrosc., 5, 474
Compagnini, G., D'Urso, L., Puglisi, O., Baratta, G. A., & Strazzulla, G. 2009, Carbon, 47, 1605
Coustenis, A., Schmitt, B., Khanna, R. K., & Trotta, F. 1999, Planet. Space Sci., 47, 1305

Cravens, T. E., et al. 2005, Geophys. Res. Lett., 32, L12108
Curtis, D. B., Hatch, C. D., Hasenkopf, C. A., Toon, O. B., Tolbert, M. A., McKay, C. P., & Khare, B. N. 2008, Icarus, 195, 792
Donnay, J. D. H., & Ondik, H. M. 1972, Crystal Data Determination Tables, Vol. 1 (3rd ed.; Washington, DC: NBS)
Drouin, D., Couture, A. R., Gauvin, R., Hovington, P., Horny, P., & Demers, H. 2001, Monte Carlo Simulation of Electron Trajectory in Solids (CASINO ver. 2.42; Sherbrooke: Univ. Sherbrooke)
Frenklach, M., Wang, H., & Rabinowitz, M. J. 1992, Prog. Energy Combust Sci., 18, 47
Gallinella, E., & Cadioli, B. 1997, Vib. Spectrosc., 13, 163
Gerakines, P. A., Bray, J. J., Davis, A., & Richey, C. R. 2005, ApJ, 620, 1140
Gerakines, P. A., Schutte, W. A., & Ehrenfreund, P. 1996, A&A, 312, 289
Griffith, C. A., et al. 2006, Science, 313, 1620
Hepp, M., & Herman, M. 1999, J. Mol. Spectrosc., 197, 56
Hudson, R. L., Moore, M. H., & Raines, L. L. 2009, Icarus, 203, 677
Hunten, D. M. 2006, Nature, 443, 669
Irle, S., & Morokuma, K. 2000, J. Chem. Phys., 113, 6139
Jackson, W. M., Faris, J., & Buccos, N. J. 1966, J. Chem. Phys., 45, 4145
Jensen, J. H., Morokuma, K., & Gordon, M. S. 1994, J. Chem. Phys., 100, 1981
Kaiser, R. I., & Roessler, K. 1998, ApJ, 503, 959
Kerkeni, B., & Clary, D. C. 2005, J. Chem. Phys., 123, 064305
Liang, M., Yung, Y. L., & Shemansky, D. E. 2007, ApJ, 661, L199
López-Moreno, J. J., et al. 2008, Geophys. Res. Lett., 35, L22104
Lorenz, R. D., et al. 2008, Geophys. Res. Lett., 35, L02206
Lunine, J. I., Stevenson, D. J., & Yung, Y. L. 1983, Science, 222, 1229
McKay, C. P., et al. 2001, Planet. Space Sci., 49, 79
Mebel, A. M., Lin, S.-H., & Chang, C.-H. 1997, J. Chem. Phys., 106, 2612
Molina-Cuberos, G. J., López-Moreno, J. J., Rodrigo, R., Lara, L. M., & O'Brien, K. 1999, Planet. Space Sci., 47, 1347
Moore, M. H., & Hudson, R. L. 1998, Icarus, 135, 518
Moore, M. H., & Hudson, R. L. 2003, Icarus, 161, 486
Mousis, O., & Schmitt, B. 2008, ApJ, 677, L67
Mumma, M. J., DiSanti, M. A., Russo, N. D., Fomenkova, M., Magee-Sauer, K., Kaminski, C. D., & Xie, D. X. 1996, Science, 272, 1310
Niemann, H. B., et al. 2005, Nature, 438, 779
Okabe, H., & McNesby, J. R. 1961, J. Chem. Phys., 34, 668
Pacansky, J., & Schrader, B. 1983, J. Chem. Phys., 78, 1033
Radebaugh, J., et al. 2008, Icarus, 194, 690
Rannou, P., Montmessin, F., Hourdin, F., & Lebonnois, S. 2006, Science, 311, 201
Russo, N. D., Mumma, M. J., DiSanti, M. A., Magee-Sauer, K., & Novak, R. 2001, Icarus, 153, 162
Russo, N. D., Vervack, R. J., Jr., Weaver, H. A., & Lisse, C. M. 2009, Icarus, 200, 271
Russo, N. D., et al. 2006, Icarus, 184, 255
Sagan, C., & Thompson, W. R. 1984, Icarus, 59, 133
Sasaki, T., Kanno, A., Ishiguro, M., Kinoshita, D., & Nakamura, R. 2005, ApJ, 618, L57
Scheer, M. D., McNesby, J., & Klein, R. 1962, J. Chem. Phys., 36, 3504
Sigurbjörnsson, Ó. F., & Signorell, R. 2008, Phys. Chem. Chem. Phys., 10, 6211
Strazzulla, G., Baratta, G. A., Domingo, M., & Satorre, M. A. 2002, Nucl. Instrum. Methods Phys. Res. B, 191, 714
Tejada, S. B., & Eggers, D. F., Jr. 1976, Spectrochim. Acta A, 32, 1557
Vinatier, S., et al. 2007, Icarus, 188, 120
Whitten, R. C., Borucki, W. J., & Tripathi, S. 2007, J. Geophys. Res., 112, E04001
Wilson, E. H., & Atreya, S. K. 2009, J. Phys. Chem. A, 113, 11221
Wisnosky, M. G., Eggers, D. F., Fredrickson, L. R., & Decius, J. C. 1983a, J. Chem. Phys., 79, 3505
Wisnosky, M. G., Eggers, D. F., Fredrickson, L. R., & Decius, J. C. 1983b, J. Chem. Phys., 79, 3513
Yung, Y. L., Allen, M., & Pinto, J. P. 1984, ApJS, 55, 465
Zheng, W., & Kaiser, R. I. 2007, Chem. Phys. Lett., 440, 229